Organometallic Perovskite Metasurfaces

Behrad Gholipour, Giorgio Adamo, Daniele Cortecchia, Harish N. S. Krishnamoorthy, Muhammad. D. Birowosuto, Nikolay I. Zheludev, and Cesare Soci*

Metamaterials allow control and tailoring of the optical response of natural materials to achieve unprecedented functionalities.[1] These artificial electromagnetic media are engineered by structuring materials on a subwavelength scale. Originally created for achieving extraordinary electromagnetic response in passive media (e.g., negative refraction, giant chirality, terahertz magnetism, and subwavelength switches),[2] metamaterials have been conventionally made out of noble plasmonic metals. Intrinsically, plasmonic metamaterials suffer from high-energy dissipation due to Ohmic losses, particularly in the near-infrared (IR) to visible spectral range, which compromise some applications.[3] All-dielectric resonant metamaterials could potentially alleviate losses, while allowing similar functionalities.[4] As the Lorenz–Mie solution to Maxwell's equations reveals,[5] dielectric structures that possess a high refractive index and a size that is comparable to or smaller than the wavelength of the incident light support strong optical resonances, known as Mie or leaky-mode resonances. As such, proper control of the resonator geometry and composition allows control of the effective permittivity and permeability of these structures. Recent work has shown that many important attributes of plasmonic metamaterials such as narrow-band resonances, magnetic response, and negative refraction can also be achieved within all-dielectric systems, presenting an attractive alternative to lossy metals. Thus far, a wide variety of dielectric metadevice functionalities such as filtering,[3,6] chirality,[7] broadband reflection,[8] focusing,[9] as well as optical magnetism,[6,10] have been demonstrated in silicon and its various alloys, as well as high index chalcogenides.[11,12] Notable applications of such dielectric structures include the realization of high-efficiency solar cells,[13] photodetectors, resonant nanoantennas,[14] and metaswitches,[15] predominantly in the near- to mid-infrared parts of the spectrum.

Here we show that, in the search for alternative dielectric photonic materials, solution-processed organometallic halide perovskites provide a high index, low-loss platform for realizing metasurfaces with high Q-factor resonances at visible frequencies (**Figure 1**a). Organolead halide perovskites are emerging solution-processable materials with outstanding optoelectronic properties.[16] Among them, methylammonium lead iodide perovskite, $CH_3NH_3PbI_3$, has proven to be an exceptional light harvester for hybrid organic–inorganic solar cells,[17] which in just a few years has achieved an impressive NREL certified power conversion efficiency over 20%, and remarkable performance in a variety of device architectures.[18] Such perovskites have been touted as a potential candidate for building-integrated photovoltaics (BIPV), which require large-area, semi-transparent solar cells.[19] Furthermore, thanks to their cost-effectiveness and ease of processing, hybrid perovskites are attracting vast interest for potential applications beyond the photovoltaic domain, such as water splitting,[20] light-emitting devices (LEDs)[21] and displays, as well as tunable lasers.[22] To obtain the wide color gamut required for these applications, research has focused on chemical tuning by varying the perovskite composition.[23] This limits the choice of materials to the natural color variation of unstructured perovskite films. Alternatively, the photonic response of materials can be effectively tuned across the visible frequency range by nanostructuring them at subwavelength scales.[12,24] Indeed, in nature many plants and animals display dramatic "structural colors" derived from astonishingly intricate spatial assemblies of intrinsically colorless biomaterials.[25] While the physics of structural coloring is in many cases well understood, replicating them remains a significant technological challenge,[26] and typically requires complex multilayer deposition or nanofabrication procedures.[27]

With the present experiments we demonstrate the first tunable-color perovskite metasurfaces consisting of nanogratings and nanoslit metamolecules etched into subwavelength (thickness ≈200 nm) $CH_3NH_3PbI_3$ films cast from solution (Figure 1b, Figures S1–S4, Supporting Information). We show that the spectral position and quality factor of the reflection resonances can be precisely engineered by varying several degrees of freedom in the geometrical parameter space, providing a simple toolset to create colored perovskite metasurfaces over the entire visible frequency range.

Dr. B. Gholipour, Dr. G. Adamo,
Dr. H. N. S. Krishnamoorthy, Prof. N. I. Zheludev,
Prof. C. Soci
Centre for Disruptive Photonic Technologies
TPI, SPMS
Nanyang Technological University
21 Nanyang Link, Singapore 637371, Singapore
E-mail: csoci@ntu.edu.sg
D. Cortecchia
Interdisciplinary Graduate School
Nanyang Technological University
Singapore 639798, Singapore
D. Cortecchia, Prof. C. Soci
Energy Research Institute @ NTU (ERI@N)
Research Techno Plaza
Nanyang Technological University
50 Nanyang Drive, Singapore 637553, Singapore
Dr. M. D. Birowosuto
CINTRA UMI CNRS/NTU/THALES 3288
Nanyang Technological University
Research Techno Plaza
50 Nanyang Drive, Border X Block, Level 6, Singapore 637553, Singapore
Prof. N. I. Zheludev
Optoelectronics Research Centre and Centre for Photonic Metamaterials
University of Southampton
SO17 1BJ, Southampton, UK
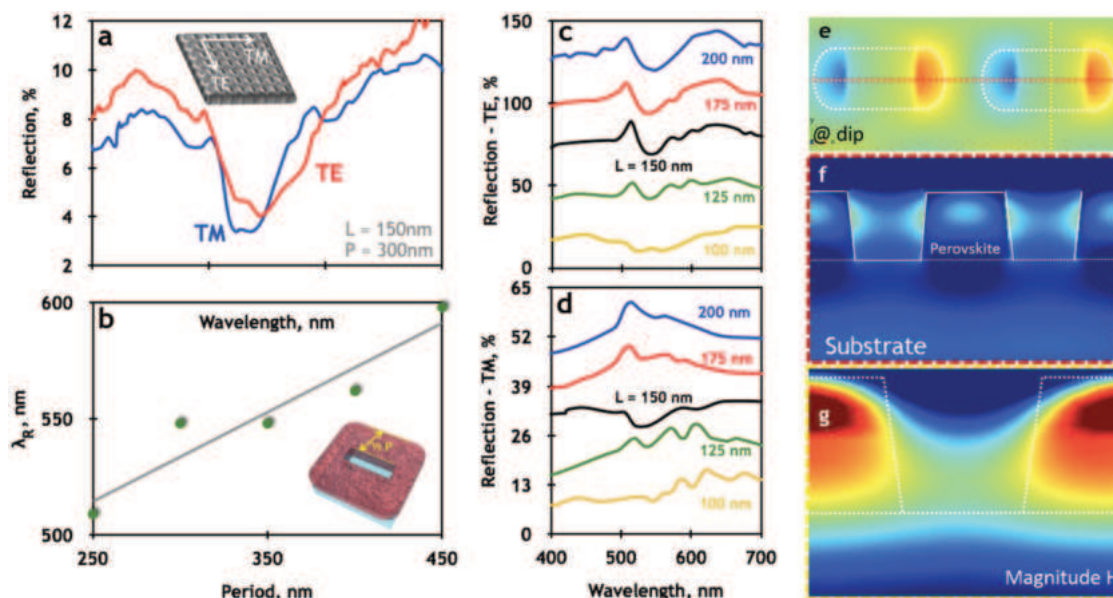
COMMUNICATION
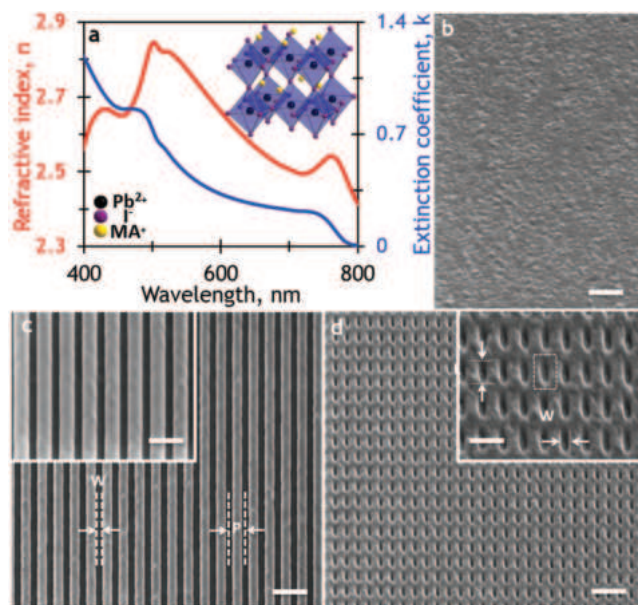
Figure 1. Optical constants and microscopy of all-organolead halide perovskite metasurfaces. a) Experimental optical constants obtained from variable angle spectroscopic ellipsometry on a representative unstructured sample (for substrate optical constants see Figure S1, Supporting Information). Inset shows the crystal structure of MAPbI$_3$, where MA = CH$_3$NH$_3^+$. The perovskite structure is formed by a 3D network of corner-sharing PbI$_6^{4-}$ octahedra, with the methylammonium cation MA$^+$ occupying the cubo-octahedral cavities. Corresponding scanning electron microscope images of b) unstructured, c) asymmetric nanograting, and d) nanoslit metamaterials fabricated in a spin-coated 200 nm film of methylammonium lead iodide perovskite (CH$_3$NH$_3$PbI$_3$).

Normal incidence reflection and transmission of unstructured subwavelength films are entirely determined by their thickness and complex refractive index. Subwavelength periodic structuring of such films introduces narrow nondiffractive resonances in reflection or transmission due to the interaction between thin film interference and grating modes.[28] These structures are nondiffractive, therefore behave as homogenous layers in the far field. Based on these principles, trihalide perovskite metasurface structures were designed to introduce pronounced resonances in their reflection properties. Perovskite films with thickness ranging from 100 to 200 nm were synthesized from organic precursors and spin-coated onto quartz substrates (see the Experimental Section). Nanograting and nanoslit metasurface patterns, with a fixed groove width (W) of ≈100 nm were milled through the perovskite layer to various depths (from 20 to 200 nm) by focused ion beam (FIB),[36] covering an area of ≈20 µm × 20 µm (see the Experimental Section). The nanograting period (P) ranged from 300 to 450 nm (Figure 1c); corresponding periods were fabricated for the nanoslits, with slit length (L) varying from 100 to 200 nm (Figure 1d).

Figure 2a,b shows the experimental and simulated reflection of representative nanograting metasurfaces for incident polarization parallel to the grooves of the grating (TE). As seen from the data, the reflectivity of nanogratings can be effectively tuned by varying the grating period. Discrepancies between experiment and finite-element simulations may be due to manufacturing imperfections (deviations from the ideal model geometry such as beveled edges of the ridges), possible stoichiometric drift in the perovskite induced by FIB milling (which may cause slight changes in the refractive index from that of the unstructured films), as well as due to slight morphological
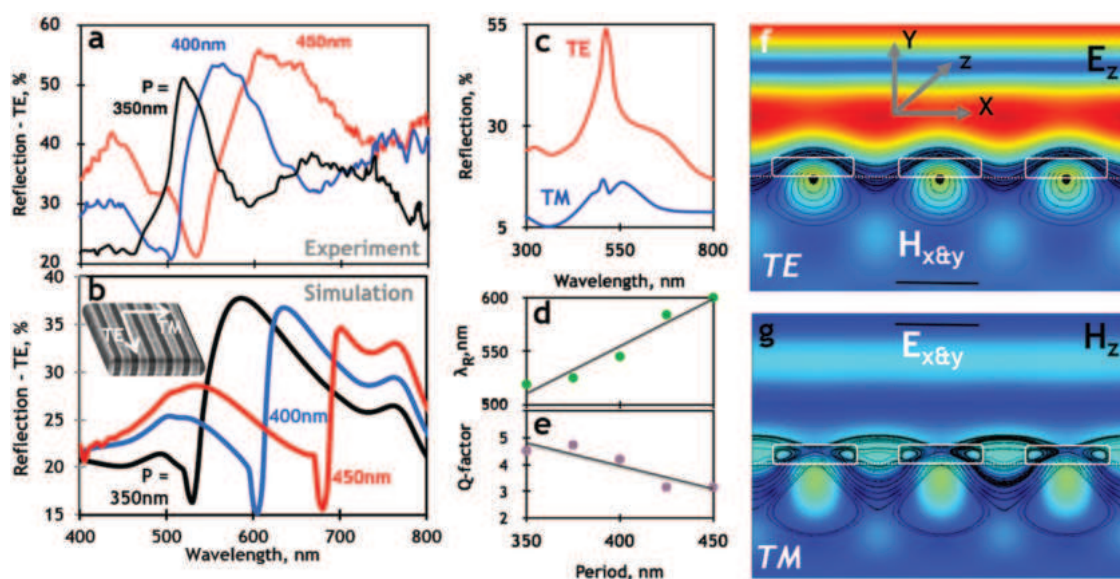
Figure 2. Optical response of perovskite nanograting metasurfaces. a) Reflection spectra for nanograting metasurfaces tuned by period from 350 to 450 nm. As the period of the metasurfaces is increased, their resonances redshift in energy and broaden, and higher order resonances start appearing, which is in agreement with, b) simulated spectra of the respective structures. c) Typical reflection spectra of TM and TE polarized light in nanograting (P = 350 nm) metasurfaces. d) Nanograting metasurfaces present tunable resonances when illuminated with TE polarized light with e) high-quality factors. Simulated electric and magnetic field distribution for f) TE and g) TM incident polarized light.

ADVANCED
SCIENCE NEWS
www.advancedsciencenews.com

ADVANCED
MATERIALS
www.advmat.de

COMMUNICATION

Figure 3. Structural tuning of the reflection properties of nanoslit metasurfaces. a) Reflection response of a nanoslit metasurface with $L = 150$ nm and $P = 300$ nm showing similar behavior for both TM and TE polarized incident light. b) Structural tuning (period 250–450 nm) of reflection spectra for TE polarized light incident on the nanoslit metasurfaces. Nanoslit metasurfaces' response can also be tuned by varying the length (in this case, from 100 to 200 nm, in 25 nm steps) of a slit metamolecule, enabling the tuning of optical response between c) TE and d) TM incident light. e) Birds-eye and cross-section view of simulated f) electric and g) magnetic field distribution for TE polarized incident light.

differences between the films used to determine optical constants by ellipsometry and the actual films used to fabricate the nanogratings.[29]

In the case of anisotropic resonators, the optical response is expected to depend on the polarization of incident light. As such, the optical response of nanograting metasurfaces is highly sensitive to polarization, with resonant peaks almost disappearing with incident polarization perpendicular to the grooves of the grating (TM), see Figure 2c. On the other hand, for TE incident polarization, the resonances in reflectivity spectra exhibit a high-quality factor of $Q > 3$ ($Q = \Delta\lambda/\lambda_R$, where λ_R is the resonance wavelength and $\Delta\lambda$ is the spectral half-maximum linewidth), and can be tuned across a range of visible frequencies by varying the grating period (Figure 2d,e).

Within dielectric metasurfaces, the distribution of electric and magnetic fields at the resonant frequencies is confined inside the nanostructured dielectric medium, due to the relatively high refractive index of the perovskite. This facilitates coupling of incident light to guided and diffracted modes in the structure, resulting in the constructive interference of light trapped inside the perovskite nanostructure (Figure 2f,g), similar to whispering-gallery or leaky-mode resonances in larger square and microdisk resonators.[30] The resonant TE response is characterized by the excitation of antiphased displacement currents (in the $\pm z$ direction) along the core and sides of each perovskite ridge, and a circulating pattern of magnetic field within the ridges. It should be noted that the field distribution in dielectric gratings is in contrast to the case of metallic gratings, where the spatial distribution of the fields is mainly concentrated at the interface metal–air or metal–substrate. This gives rise to the strong resonances in TE, rather than TM mode of our perovskite nanograting structures.[31] Conversely, the TM response results from displacement currents circulating in the xy plane (forming magnetic dipoles oriented along z).

While nanograting metasurfaces present an attractive anisotropic resonant geometry, with distinct response in the TM and TE polarizations, many practical applications require independent control of the polarization response. To this end, we explored perovskite nanoslit metasurfaces that present an additional degree of geometrical freedom, the slit length (L), which enables the design of metamolecules with variable anisotropy in the TM and TE polarizations (**Figure 3**a). Similar to their nanograting counterparts, the optical resonances of nanoslit metasurfaces for TE incident polarization appear at spectral positions directly proportional to their respective periods (Figure 3b). As the period of the metasurfaces is increased, their resonances red shift in energy and broaden, which is in agreement with simulated spectra of the respective structures (Figure S5, Supporting Information). The optical response of nanoslit metasurfaces for TM incident light can be effectively tuned by varying the length of the nanoslits thus allowing control over the anisotropy of the structures: for more isotropic geometries of the metamolecules (e.g., $L = 150$ nm, $P = 300$ nm), the response to TM and TE incident light becomes almost identical (**Figure 4**c,d). Governed by the same principles as the nanograting metasurfaces, the distribution of electric and magnetic fields at the resonant frequencies is strongly confined within the dielectric perovskite films (Figure 3e,f). Similarly, the enhancement of reflectivity in particular spectral windows results from the interplay between the single nanoslit scattering resonances and the coupling to guided and diffracted modes in the perovskite film. In this case, both TE and TM responses are characterized by the excitation of antiphased displacement currents (in the $\pm z$ direction), along the edges of the
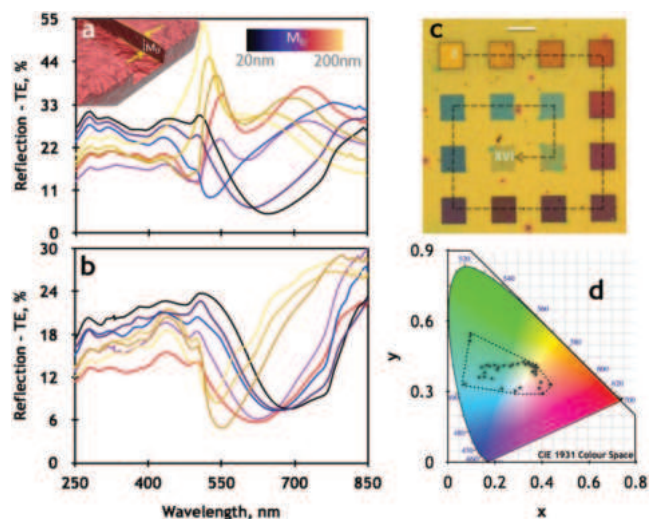
Figure 4. Tunable color perovskite metasurfaces. Reflection spectra of a) nanograting, b) nanoslit metasurfaces, with varying mill depths from $d \approx 200$ nm (fully etched) to $d \approx 20$ nm etch depth; c) corresponding unpolarized optical microscope image of nanograting metasurfaces ($P = 350$ nm) with 19 different mill depths ranging from ≈ 200 nm (I) to ≈ 20 nm (XVI) mill depth. Scale bar indicates 20 µm. d) CIE color palette with marked points for a selection of the nanograting metasurfaces created.

nanoslits and leaky modes in the perovskite/substrate interface (Figure 3e), alongside a circulating pattern of magnetic field within the perovskite (Figure 3g).

In addition to the wide palette of structural resonances achievable in thin perovskite films by adjusting nanograting periods and slit metamolecule geometries, variations in the milling depth (d) can provide access to a significant portion of the visible color space. Figure 4a,b shows the spectral response of nanograting and nanoslit metasurfaces with constant period of 350 nm to TE incident light polarization, as a function of milling depths into the perovskite film. In the case of the nanograting metasurfaces, for example, the pronounced reflection resonance observed at high milling depth red shifts and fades off with decreasing milling depth, in favor of a spectral response dominated by a broad dip matching more closely to the response of the flat perovskite film. As illustrated in the optical microscope image and corresponding CIE 1931 color space in Figure 4c,d (Figure S6, Supporting Information, for nanoslits), the color variation from that of the unstructured perovskite is dramatic, covering a wide range of color coordinates from yellow, red, green to blue. As opposed to coloring achieved by chemical and compositional variation of the perovskite film, the vibrant coloring observed from nanograting and nanoslit metasurfaces is completely determined by structural design, and can be made dependent or independent on the polarization of incident light by the choice of metamolecule geometry. The parameter space for metamolecule design is almost unlimited and different resonator geometries will undoubtedly extend the accessible color range shown for a selection of various metasurfaces fabricated. That said, "pure" colors found at the boundaries of the CIE 1931 standard color space could be a significant challenge, as they require suppression of reflectivity across all but a narrow band of the visible spectrum.
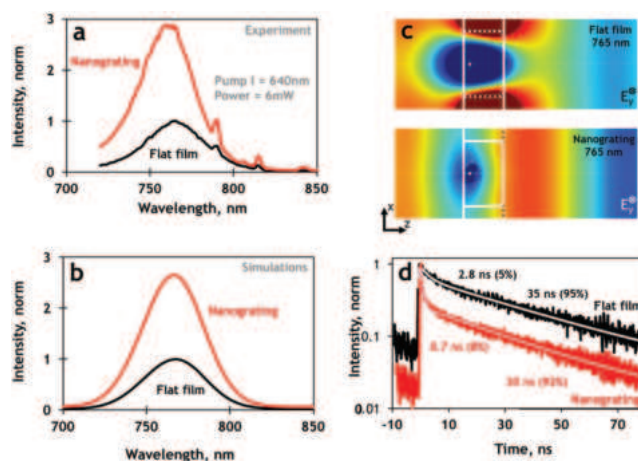
Figure 5. Perovskite luminescence enhancement controlled by metamaterial design. a) Photoluminescence (PL) of a grating milled into a perovskite film ($P = 350$ nm), showing a clear enhancement of ≈ 3 when compared to an unstructured film. TE excitation at $\lambda = 640$ nm and unpolarized detection. b) Simulated emission spectra of unpolarized light for the flat film and the nanograting and c) field maps of γ-oriented dipole radiation in the case of the flat film (top panel) and the nanograting (bottom panel): radiation is stronger in the nanograting case. d) Time-resolved PL emission decay at the spectral maximum for the two corresponding cases. TE excitation at $\lambda = 640$ nm and unpolarized detection centered at $\lambda = 760$ nm. Deconvolution fitting of double exponential decay with instrument response function (best-fit parameters reported in the figure).

Aside from structural coloring, which may be utilized to optimize the linear absorption and reflection properties of perovskite films used in photovoltaic applications, subwavelength resonators could also be employed to modify the light emission properties of perovskite LEDs and lasers. Methylammonium lead iodide, along with similar hybrid perovskites, emits strong and broad photoluminescence (PL) around its optical bandgap energy of ≈ 1.6 eV. As demonstrated in **Figure 5**, the nanostructuring of a perovskite thin film with the nanograting structure presented earlier leads to a clear enhancement of PL intensity (Figure 5a), with enhancement factor of ≈ 3. The luminescence enhancement is a clear manifestation of the Purcell effect, and can be controlled by the metamaterial's design. Indeed, the spontaneous emission decay rate is proportional to the density of photon states that the photonic environment offers for radiative decay. The far-field photoluminescence enhancement can be well reproduced by full-wave electromagnetic simulations (Figure 5b) of infinitesimally small dipoles placed within the perovskite, using spectral distribution of emitters from steady-state PL, with radiation strength proportional to the simulated optical absorption at dipole locations (see details in the Experimental Section). This also helps in understanding the role played by the electromagnetic modes of the nanostructured high refractive index dielectric metamaterial in the reradiation of the light generated in the perovskite (Figure 5c); the modes created due to nanostructuring of the film enhances light–matter interaction and increases the density of photon states.[32] Time-resolved PL measurements indicate that the prompt radiative decay rate in the nanogratings ($\tau \approx 0.7$ ns) is four times larger than in the unstructured film ($\tau \approx 2.8$ ns), consistent with

the Purcell enhancement factor determined from steady-state PL measurements, which do not account for nonradiative processes (Figure 5d).

In conclusion, we provided the first demonstration of all-dielectric, solution-processed perovskite metasurfaces, with structural color and radiative emission properties tunable on demand. We showed that nanograting and nanoslits are simple, versatile structures to engineer Mie optical resonances and dramatically change light absorption and emission in perovskite subwavelength films. Perovskite metasurfaces can be produced over large areas through structuring techniques such as nano-imprint lithography, microcontact printing, or nanoembossing. These low-cost mass manufacturing alternatives to ion beam milling and reactive etching techniques, will minimize process related degradation and contamination in the active perovskite layer during patterning, which will ensure long-term stability of the fabricated structures. Moreover, the advancement of synthetic strategies will provide new ways to achieve long-term stability, like in recent 2D perovskites with Ruddlesden–Popper phases.[33] This will open up several opportunities for light management in large-area metal–organic perovskite devices. For instance, the tunability of the vibrant structural color demonstrated across the entire visible palette may be used to increase the power conversion efficiency of broadband solar cells or vary the appearance of semitransparent, building integrated photovoltaics. Purcell enhancement of photo-/electroluminescence may be exploited to improve the efficiency of large-area hybrid perovskite LEDs or be extended to the emerging class of white-light-emitting perovskite compounds (e.g., $EDBEPbX_4$, where X = Cl, Br)[34] to realize full-color active displays with a single emissive material. Dielectric metasurfaces also offer the possibility to design mode confinement and polarization dependence of the optical response, which may be exploited to further optimize light absorption in solar cells and improve light extraction and directivity of light-emitting devices and displays.

Experimental Section

Sample Preparation: Synthesis of Methylammonium Iodide (MAI): Hydroiodic acid (57% wt in water, Sigma-Aldrich) was slowly dropped into a methylamine solution (CH_3NH_2, 40% in methanol, Tokyo Chemical Industry, Co., Ltd.) in 1:1 molar ratio. After 2 h of reaction in an ice-cooled bath, the solvent was removed by a rotary evaporator. The resulting powder was dissolved in hot ethanol and recrystallized with diethylether (6× times) for purification. The resulting MAI white powder was dried in a vacuum oven and stored in an N_2 environment.

Deposition of Perovskite Films and Characterization: Methylammonium lead iodide $MAPbI_3$ was deposited by spin-coating using lead acetate trihydrate ($Pb(Ac)_2 \cdot 3H_2O$, 99.999%, Sigma-Aldrich) as inorganic precursor. Dimethylformamide (DMF) solutions with concentration 20% wt of $Pb(Ac)_2 \cdot 3H_2O$ and excess of MAI (3 equivalents) were prepared and left under magnetic stirring at 100 °C. The mixed hot solution was spin-coated on glass substrate at 5000 rpm, 30 s. The resulting film was then annealed on a hotplate at 100 °C for 10 min. X-ray diffraction characterization was performed on a BRUKER D8 ADVANCE with Bragg–Brentano geometry using Cu Kα radiation ($\alpha = 1.54056$ Å), step increment of 0.02°, and 1 s of acquisition time. An UV–vis–NIR spectrophotometer (UV3600, Shimadzu) equipped with integrating sphere was used for optical characterization of the unstructured films.

Focused Ion Beam Milling: Arrays of nanoslit and grating metasurfaces were patterned on a spin-coated perovskite film on a quartz substrate using a Helios 600 NanoLab FIB. Currents used were ≤19 pA. The lateral dimension of each fabricated sample was 20×20 μm.

Optical Characterization: Ellipsometry: The optical constants of the perovskite film and substrate were determined from spectroscopic ellipsometry measurements using a J. A. Woollam alpha-SE ellipsometer. Analysis and modeling of the ellipsometry data was done using the J.A. Woollam CompleteEASE software. The ellipsometry data were collected in the spectral range 400–800 nm, at three different angles (65°, 70°, and 75°). First, the optical constants of the quartz substrate were determined by performing ellipsometry measurements on it and modeling the data using a Cauchy dispersion formula. Subsequently, ellipsometry measurements were performed on the perovskite sample (200 nm thick $CH_3NH_3PbI_3$ film) deposited on the quartz substrate and its optical constants were determined by fitting the ellipsometry data using a B-spline model that describes the real and imaginary parts of optical constant as continuous functions of wavelength obeying the Kramers–Kronig relations. The optical constants of the perovskite film in literature[37] were used as the starting point for the B-spline model.

Microspectrophotometry: The normal-incidence reflection characteristics of the perovskite metasurfaces were quantified, for incident polarizations parallel and perpendicular to the grating and slit lines (TE and TM orientations, respectively), using a microspectrophotometer (Jasco MV2000), through a 36× objective with a circular sampling aperture size of 15 μm × 15 μm.

Photoluminescence: Microphotoluminescence measurements were performed using free space excitation and collection through a visible–near infrared microscope objective (Olympus 80×, NA = 0.90). The samples were excited with a ps-pulsed laser diode emitting at 640 ± 5 nm wavelength with 10 MHz repetition rate, focused to a beam size of 2 μm. Luminescence was detected using a Peltier-cooled photomultiplier tube (Hamamatsu H7422 series) coupled to a grating spectrometer (Edinburgh Instruments F900 and Bentham TMS300). Time-resolved decay traces were acquired by a time-correlated single-photon counting acquisition module (Edinburgh Instruments, TCC900) at selected wavelength of 760 ± 5 nm.

Numerical Simulations: Finite Element Simulations: Reflection spectra and field maps were generated by full-wave electromagnetic simulations using COMSOL Multiphysics. Experimental ellipsometric values were used to describe both the silica substrate (Figure S1, Supporting Information) and the perovskite film. The samples were described as infinitely extended by using periodic boundary conditions and illuminated at normal incidence. Within these simulations, the film thickness had to be varied to obtain a good fit to the data of different experimental sets, which may reflect the intrinsic variability of the perovskite films across the substrate, sample-to-sample variability of the thickness, or actual variation of the thickness induced by the ion milling process.

The emission spectra were simulated by placing an array of infinitesimally small dipoles within the perovskite film, with spectral distribution mimicking the steady-state PL spectrum of the flat perovskite film. The total emission power was determined by averaging individual dipole contributions at each wavelength, weighted by the simulated field intensity generated at the dipole position by the pump beam ($\lambda = 640$ nm)[35] to account for the absorption.

Supporting Information

Supporting Information is available from the Wiley Online Library or from the author. Following a one year period of embargo, the data from this paper can be obtained from the University of Southampton ePrints research repository, http://dx.doi.org/10.5258/SOTON/403138.

Acknowledgements

[1] N. I. Zheludev, Y. S. Kivshar, *Nat. Mater.* **2012**, *11*, 917.

[2] a) D. R. Smith, *Science* **2004**, *305*, 788; b) B. Gholipour, J. Zhang, K. F. MacDonald, D. W. Hewak, N. I. Zheludev, *Adv. Mater.* **2013**, *25*, 3050; c) H.-T. Chen, W. J. Padilla, J. M. O. Zide, A. C. Gossard, A. J. Taylor, R. D. Averitt, *Nature* **2006**, *444*, 597.

[3] Y. Yang, I. I. Kravchenko, D. P. Briggs, J. Valentine, *Nat. Commun.* **2014**, *5*, 5753.

[4] a) A. Boltasseva, H. A. Atwater, *Science* **2011**, *331*, 290; b) S. Jahani, Z. Jacob, *Nat. Nanotechnol.* **2016**, *11*, 23.

[5] A. P. Vasudev, J. A. Schuller, M. L. Brongersma, *Opt. Express* **2012**, *20*, A385.

[6] J. Zhang, K. F. MacDonald, N. I. Zheludev, *Opt. Express* **2013**, *21*, 26721.

[7] C. Wu, N. Arju, G. Kelp, J. A. Fan, J. Dominguez, E. Gonzales, E. Tutuc, I. Brener, G. Shvets, *Nat. Commun.* **2014**, *5*, 3892.

[8] P. Moitra, B. A. Slovick, Z. G. Yu, S. Krishnamurthy, J. Valentine, *Appl. Phys. Lett.* **2014**, *104*, 171102.

[9] P. R. West, J. L. Stewart, A. V. Kildishev, V. M. Shalaev, V. V. Shkunov, F. Strohkendl, Y. A. Zakharenkov, R. K. Dodds, R. Byren, *Opt. Express* **2014**, *22*, 26212.

[10] a) J. C. Ginn, I. Brener, D. W. Peters, J. R. Wendt, J. O. Stevens, P. F. Hines, L. I. Basilio, L. K. Warne, J. F. Ihlefeld, P. G. Clem, M. B. Sinclair, *Phys. Rev. Lett.* **2012**, *108*. b) E. Semouchkina, D. H. Werner, P. L. Werner, C. Pantano, D. H. Kwon, presented at *IEEE Antennas and Propagation Society Int. Symp.*, June **2009** c) E. Semouchkina, D. H. Werner, P. L. Werner, C. Pantano, D. H. Kwon, presented at *IEEE Antennas and Propagation Society Int. Symp.*, June **2009**. d) E. Semouchkina, D. H. Werner, P. L. Werner, C. Pantano, D. H. Kwon, presented at *IEEE Antennas and Propagation Society Int. Symp.*, July **2009**.

[11] Q. Wang, E. T. F. Rogers, B. Gholipour, C.-M. Wang, G. Yuan, J. Teng, N. I. Zheludev, *Nat. Photonics* **2015**, *10*, 60.

[12] S. J. Tan, L. Zhang, D. Zhu, X. M. Goh, Y. M. Wang, K. Kumar, C.-W. Qiu, J. K. W. Yang, *Nano Lett.* **2014**, *14*, 4023.

[13] L. Cao, P. Fan, A. P. Vasudev, J. S. White, Z. Yu, W. Cai, J. A. Schuller, S. Fan, M. L. Brongersma, *Nano Lett.* **2010**, *10*, 439.

[14] A. E. Krasnok, P. A. Belov, A. E. Miroshnichenko, A. I. Kuznetsov, B. S. Luk'yanchuk, Y. S. Kivshar, *Progress in Compact Antennas*, Intech, **2014**.

[15] a) A. Karvounis, B. Gholipour, K. F. MacDonald, , N. I. Zheludev, *Appl. Phys. Lett.* **2016**, *109*, 051103; b) A. Karvounis, J.-Y. Ou, W. Wu, K. F. MacDonald, N. I. Zheludev, *Appl. Phys. Lett.* **2015**, *107*, 191110; c) J. Zhang, K. F. MacDonald, N. I. Zheludev, *Light: Sci. Appl.* **2013**, *2*, e96.

[16] S. D. Stranks, G. E. Eperon, G. Grancini, C. Menelaou, M. J. P. Alcocer, T. Leijtens, L. M. Herz, A. Petrozza, H. J. Snaith, *Science* **2013**, *342*, 341.

[17] M. A. Green, A. Ho-Baillie, H. J. Snaith, *Nat. Photonics* **2014**, *8*, 506.

[18] a) T. Salim, S. Sun, Y. Abe, A. Krishna, A. C. Grimsdale, Y. M. Lam, *J. Mater. Chem. A* **2015**, *3*, 8943; b) X. Li, D. Bi, C. Yi, J. D. Decoppet, J. Luo, S. M. Zakeeruddin, A. Hagfeldt, M. Gratzel, *Science* **2016**, *353*, 58.

[19] G. E. Eperon, V. M. Burlakov, A. Goriely, H. J. Snaith, *ACS Nano* **2014**, *8*, 591.

[20] J. Luo, J. H. Im, M. T. Mayer, M. Schreier, M. K. Nazeeruddin, N. G. Park, S. D. Tilley, H. J. Fan, M. Gratzel, *Science* **2014**, *345*, 1593.

[21] X. Y. Chin, D. Cortecchia, J. Yin, A. Bruno, C. Soci, *Nat. Commun.* **2015**, *6*, 7383.

[22] G. Xing, N. Mathews, S. S. Lim, N. Yantara, X. Liu, D. Sabba, M. Grätzel, S. Mhaisalkar, T. C. Sum, *Nat. Mater.* **2014**, *13*, 476.

[23] G. E. Eperon, S. D. Stranks, C. Menelaou, M. B. Johnston, L. M. Herz, H. J. Snaith, *Energy Environ. Sci.* **2014**, *7*, 982.

[24] J. Zhang, J.-Y. Ou, N. Papasimakis, Y. Chen, K. F. MacDonald, N. I. Zheludev, *Opt. Express* **2011**, *19*, 23279.

[25] P. Vukusic, J. R. Sambles, *Nature* **2003**, *424*, 852.

[26] M. Kolle, P. M. Salgard-Cunha, M. R. J. Scherer, F. Huang, P. Vukusic, S. Mahajan, J. J. Baumberg, U. Steiner, *Nat. Nanotechnol.* **2010**, *5*, 511.

[27] a) W. Zhang, M. Anaya, G. Lozano, M. E. Calvo, M. B. Johnston, H. Míguez, H. J. Snaith, *Nano Lett.* **2015**, *15*, 1698; b) K. Kumar, H. Duan, R. S. Hegde, S. C. W. Koh, J. N. Wei, J. K. W. Yang, *Nat. Nanotechnol.* **2012**, *7*, 557; c) X. M. Goh, Y. Zheng, S. J. Tan, L. Zhang, K. Kumar, C.-W. Qiu, J. K. W. Yang, *Nat. Commun.* **2014**, *5*, 5361.

[28] G. D'Aguanno, D. de Ceglia, N. Mattiucci, M. J. Bloemer, *Opt. Lett.* **2011**, *36*, 1984.

[29] M. A. Green, Y. Jiang, A. M. Soufiani, A. Ho-Baillie, *J. Phys. Chem. Lett.* **2015**, *6*, 4774.

[30] a) A. W. Poon, F. Courvoisier, R. K. Chang, *Opt. Lett.* **2001**, *26*, 632; b) K. Vahala, *Optical Microcavities (Advanced Series in Applied Physics)*, 1st Ed., World Scientific Publishing, Singapore, **2004**.

[31] S. J. Kim, I. Thomann, J. Park, J.-H. Kang, A. P. Vasudev, M. L. Brongersma, *Nano Lett.* **2014**, *14*, 1446.

[32] M. Decker, I. Staude, I. I. Shishkin, K. B. Samusev, P. Parkinson, V. K. A. Sreenivasan, A. Minovich, A. E. Miroshnichenko, A. Zvyagin, C. Jagadish, D. N. Neshev, Y. S. Kivshar, *Nat. Commun.* **2013**, *4*, 2949.

[33] a) H. Tsai, W. Nie, J.-C. Blancon, C. C. Stoumpos, R. Asadpour, B. Harutyunyan, A. J. Neukirch, R. Verduzco, J. J. Crochet, S. Tretiak, L. Pedesseau, J. Even, M. A. Alam, G. Gupta, J. Lou, P. M. Ajayan, M. J. Bedzyk, M. G. Kanatzidis, A. D. Mohite, *Nature* **2016**, *536*, 312; b) N. Wang, L. Cheng, R. Ge, S. Zhang, Y. Miao, W. Zou, C. Yi, Y. Sun, Y. Cao, R. Yang, Y. Wei, Q. Guo, Y. Ke, M. Yu, Y. Jin, Y. Liu, Q. Ding, D. Di, L. Yang, G. Xing, H. Tian, C. Jin, F. Gao, R. H. Friend, J. Wang, W. Huang, *Nat. Photonics* **2016**, *10*, 699.

[34] J. Y. D. Cortecchia, P. Lova, S. Mhaisalkar, G. G. Gurzadyan, A. Bruno, C. Soci, *arxiv:1603.01284* **2016**.

[35] A. Rose, T. B. Hoang, F. McGuire, J. J. Mock, C. Ciracì, D. R. Smith, M. H. Mikkelsen, *Nano Lett.* **2014**, *14*, 4797.

[36] M. S. Alias, I. Dursun, D. Shi, M. I. Saidaminov, E. M. Diallo, D. Priante, T. K. Ng, O. M. Bakr, B. S. Ooi, *J. Vac. Sci. Technol. B* **2015**, *33*, 051207.

wileyonlinelibrary.com